Journal of Materials Chemistry A

Ionization of Hole-Transporting Materials as a Method for Improving the Photovoltaic Performance of Perovskite Solar Cells

Journal:	*Journal of Materials Chemistry A*
Manuscript ID	TA-ART-10-2023-006427.R1
Article Type:	Paper
Date Submitted by the Author:	15-Dec-2023
Complete List of Authors:	Tingare, Yogesh; National Taipei University of Technology, Institute of Organic and Polymeric Materials/Research and Development Center for Smart Textile Technology Lin, Chien-Hsiang ; National Central University, Department of Chemistry Su, Chaochin; National Taipei University of Technology, Institute of Organic and Polymeric Materials Chou, Sheng-Chin ; National Taipei University of Technology, Institute of Organic and Polymeric Materials/Research and Development Center for Smart Textile Technology Hsu, Ya-Chun ; National Taipei University of Technology, Institute of Organic and Polymeric Materials/Research and Development Center for Smart Textile Technology Ghosh, Dibyajyoti; Indian Institute of Technology Delhi, Chemistry Lai, Ning-Wei; National Taipei University of Technology, Institute of Organic and Polymeric Materials/Research and Development Center for Smart Textile Technology Lew, Xin-Rui; National Central University, Chemistry Tretiak, Sergei; Los Alamos National Laboratory, Theoretical Division; Los Alamos National Laboratory, Center for Integrated Nanotechnologies, Materials Physics and Application Division Tsai, Hsinhan; Los Alamos National Laboratory, Center for Integrated Nanotechnologies, Materials Physics and Application Division; University of California Berkeley, Department of Chemistry Nie, Wanyi; Los Alamos National Laboratory, Center for Integrated Nanotechnologies, Materials Physics and Application Division; University at Buffalo, Department of Physics, The State University of New York. Li, Wen-Ren; National Central University, Department of Chemistry

ARTICLE

Ionization of Hole-Transporting Materials as a Method for Improving the Photovoltaic Performance of Perovskite Solar Cells

Received 00th January 20xx,
Accepted 00th January 20xx

DOI: 10.1039/x0xx00000x

Yogesh S. Tingare,[a] Chien-Hsiang Lin,[b] Chaochin Su,*[a] Sheng-Chin Chou,[a] Ya-Chun Hsu,[a] Dibyajyoti Ghosh,*[c] Ning-Wei Lai,[a] Xin-Rui Lew,[b] Sergei Tretiak,[d,e] Hsinhan Tsai,*[f] Wanyi Nie,*[e,g] and Wen-Ren Li*[b]*

In the operating mechanisms of perovskite solar cells, hole-transporting materials (HTMs) facilitate directional charge transfer and electron blocking. In addition, HTMs are also important in forming the perovskite layers for inverted perovskite solar cells, improving device efficiency. We present a method for increasing efficiency by ionizing HTMs, introducing defect-passivating abilities, improved interfacial properties, and ideal surface topographies. Compared to their non-ionized counterpart, the ionic HTMs have well-matched energy levels and smooth perovskite layers, resulting in higher short-circuit current densities. These experimental findings are corroborated by atomistic first principle electronic structure calculations of model perovskite systems. Furthermore, we conducted a comparative study of different ionizing counter anions for HTMs. The iodide-based ionic HTM, **PMO-I**, has a maximum efficiency of 20.46%, 1.71% higher than that of the non-ionic HTM, **PMO** (18.75%).

Introduction

Perovskite solar cells (PSCs) have emerged as one of the most promising photovoltaic technologies, with a power conversion efficiency (PCE) exceeding 25.5%.[1-5] Such excellent optoelectronic properties of perovskite light-absorbing materials are attributed to broad absorption spectra with high absorption coefficients, long carrier diffusion lengths, high carrier mobilities, and low exciton binding energy ambipolar charge transport. These are the primary factors responsible for PSC's high efficiency.[6-14] Apart from the high PCE, other advantages of PSCs include the ease of processing and inexpensive manufacturing cost, particularly with the inverted (*p–i–n*) architecture, which can be helpful when contemplating commercialization.[15-19] However, inverted PSCs have made less progress than traditional (*n-i-p*) PSC architectures.[20] One factor limiting the development of the inverted structures is a lack of proper interfacial contacts, such as hole-transporting materials (HTMs).[3, 21] Suitable HTMs are essential components in PSC architectures because they help improve overall efficiency by preventing electronic recombination and decreasing perovskite degradation through interfacial modification.[22, 23] Inorganic and organic molecules are the two types of HTMs employed in PSCs.[24-27] Inorganic HTMs such as NiO, CuSCN, Cu_2O, CuI, and graphene oxide show improved electrical properties and provide excellent efficiencies and stabilities to PSCs.[28-32] However, their low intrinsic conductivities and surface defects, as well as the requirement for stringent processing conditions, are the detrimental factors for using in PSCs.[25, 26, 33] Organic-based HTMs, on the other hand, with such benefits as structural versatility, high purity, low cost, and customizable energy levels, can have outstanding processability for simple one-step solution processes at low temperatures.[22, 23] Nonetheless, the advancement of PSCs depends on resolving critical issues, such as achieving even higher efficiency and long-term stability.[34] An appropriate HTM layer can come in handy to resolve these issues. Therefore, finding suitable HTM candidates has become essential for building competitive PSC devices.[35]

Many HTMs based on organic polymeric, metal-organic, and abundant small organic molecular compounds, have been developed for PSC applications.[35-44] These HTMs have variety of structures (X-type, Y-type, or a liner) as well as templets (donor-π-donor(D-π-D), donor-acceptor (D-A) or donor-acceptor-donor (D-A-D).[45-52] The majority of *n-i-p* and *p–i–n* PSC devices are based on cutting-edge HTMs such as 2,2′,7,7′-tetrakis(N,N-di-pmethoxyphenylamine)-9,9′-spirobifuorene (**Spiro-OMeTAD**),[53] which can be classified as X-type with D-π-D templet, and polymeric HTMs such as poly(3,4-ethylenedioxythiophene) doped with poly(styrenesulfonate) [**PEDOT:PSS**],[54] respectively. New strategies for designing and synthesizing high-performance HTMs are in progress.[22, 47, 51] Research exploring these new HTMs aims to replace **Spiro-OMeTAD** and **PEDOT:PSS**, which exhibit unfavorable properties such as limited long-term stability, high production cost, and moderate hole conductivity without doping.[54-56] Excellent hole conductivity, desirable solubility in selected organic solvents, high chemical, photothermal, and morphological stability, and simple synthesis and

[a] *Institute of Organic and Polymeric Materials/Research and Development Center for Smart Textile Technology, National Taipei University of Technology, Taipei-106344, Taiwan. E-mail: f12098@ntut.edu.tw; f10913@mail.ntut.edu.tw*
[b] *Department of Chemistry, National Central University, Zhongli-32001, Taiwan. E-mail: ch01@ncu.edu.tw*
[c] *Department of Chemistry and Department of Materials Science and Engineering (DMSE), Indian Institute of Technology, Delhi, Hauz Khas, New Delhi-110016, India. E-mail: dibyajyoti@iitd.ac.in*
[d] *Theoretical Division, Los Alamos National Laboratory, Los Alamos National Laboratory, Los Alamos, NM-87545, USA.*
[e] *Center for Integrated Nanotechnologies, Materials Physics and Application Division, Los Alamos National Laboratory, Los Alamos, NM-87545, USA.*
[f] *Department of Chemistry, University of California, Berkeley, Berkeley, CA 94720. E-mail: hsinhantsai@berkeley.edu*
[g] *Department of Physics, University at Buffalo, The State University of New York, Buffalo, NY 14260, USA. E-mail: wanyinie@buffalo.edu*
Electronic Supplementary Information (ESI) available: DOI: 10.1039/x0xx00000x

purification techniques for up-scaling and decreased manufacturing costs, contribute to the design of effective HTMs.[57-59]

Heteroatoms comprising moieties have recently gained interest as an exciting unit for constructing efficient HTMs for inverted PSCs.[60-62] Pyridine a Lewis base, is one of these heteroatoms candidates.[63, 64] When inserted into the HTMs core, it was found to successfully passivate interface defects by coordinating its nitrogen to lead ion vacancies, which improves hole extraction and transport capabilities.[65-67] Additionally, using an electron-deficient heteroatom in the HTM gives a D-A-D configuration structure, which has tunable optical and electrical properties and improved charge carrier transport.[68-70] Further, various organic compounds with an X-type structure,[45, 48, 71, 72] including the common **Spiro-OMeTAD**, with various functional cores and di- or tri-phenylamine units as side arms, have proven to be effective HTMs for PSCs.[47, 73, 74] The symmetric X-type arrangement can improve backbone π-π stacking interactions, which is beneficial in achieving high hole mobility.[75] Inverted PSCs also have the HTM sandwiched between the ITO and absorber layers. It would be advantageous to build an HTM that, in conjunction with effective hole transport, can promote the formation of a good perovskite layer and improve PSC efficiency. Incorporating the ionic character and increasing hydrophilicity into HTMs can improve their material properties and facilitate the growth of perovskite layers for boosting performance.[76] The sulfoxide anion can affect the crystallization of perovskites,[77] whereas the perovskite is known to become more stable when doped with KSCN.[78] On the other hand, the iodide can efficiently passivate perovskite trap states.[79] Given these advantages, we selected these anions to induce hydrophilicity in the HTM and conducted comparative studies on their overall PSC performance.

Inspired by the abovementioned factors, we synthesized D-A-D configured and X-type ionic multifarious HTMs (**PMO-MeSO$_4$**, **PMO-SCN**, and **PMO-I**) using pyrazine, a dinitrogen-containing heterocyclic aromatic organic molecule, as a structural core element (Figure 1). To validate the benefits of ionic characteristics in HTM, we studied and compared their non-ionic derivative **PMO** (Scheme 1). These HTMs are flanked by four triarylamine arms obtained by simple synthesis and are intended to apply as dopant-free hole transport in inverted PSCs. Across various metrics, such as economical synthesis, good hole mobility, high solubility in the desired organic solvent, high short-circuit current density (J_{SC}) and open-circuit voltage (V_{OC}), and long-term stability in PSCs, using a thin layer of these charged HTMs outperformed the standard **PEDOT:PSS**. One reason for such a strong performance could be the ionization of one of the nitrogen molecules, which could deepen the highest occupied molecular orbital (HOMO) energy levels,[80] increase hydrophobicity, and facilitate formation of large-grained perovskites, resulting in enhanced V_{OC} and J_{SC}, and thus higher PCE.[81-83] Furthermore, ionic entities can provide a passivation effect that can reduce the defect density on the interfaces. Additionally, its symmetric X-type structure may provide π-π stacking interactions, which is beneficial in achieving high hole mobility.[84] Further, the pyrazine core generates D-A-D templet HTM, which has proven to improve charge carrier transport by providing well-matched energy levels to the perovskite valence band.[68-70] The rational designs of **PMO**-based HTMs shows enhanced PCE and then its parent **PMO** structure with improved J_{SC} and higher V_{OC}. We attribute the interface passivation with **PMO**-based HTM that improves the device performance and supported by first principle density function theory simulation. As a result, the optimized PSCs incorporated with **PMO-I** exhibits a champion PCE of 20.46%, among all other **PMO**-base HTMs with well-matched energy levels, resulting in improved charge transfer and electron blocking capabilities.

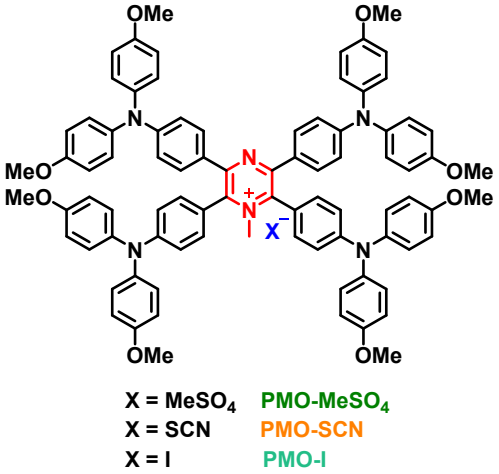

Figure 1. Molecular structure of **PMO**-MeSO4, **PMO-SCN**, and **PMO-I**.

Results and discussion

The synthetic routes of **PMO**-based HTMs (**PMO**, **PMO-MeSO$_4$**, **PMO-SCN**, and **PMO-I**) are simple and straightforward (Scheme 1). The electron-deficient 2,3,5,6-tetrakis(4-bromophenyl) pyrazine core (2) was synthesized by treating 4,4'-dibromobenzoin 1 with ammonium acetate.[85] The four bis(4-methoxyphenyl)amines

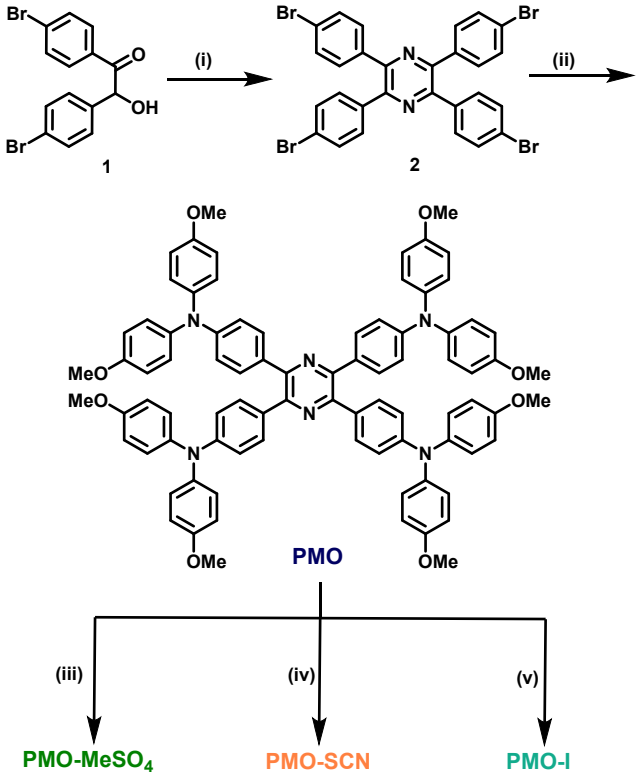

Scheme 1. Synthesis of **PMO**, **PMO-MeSO$_4$**, **PMO-SCN**, and **PMO-I**. (i) NH_4OAc, 80 °C, 1h; (ii) bis(4-methoxyphenyl)amines, *t*-BuONa, $Pd(OAc)_2$, P(*t*-Bu)$_2$, toluene, reflux, 12h; (iii) $(CH_3)_2SO_4$, dioxane, 120 °C, 12h; (iv) KCN, $(CH_3)_2SO_4$, dioxane, 120 °C, 12h; (v) KI, $(CH_3)_2SO_4$, dioxane, 120 °C, 12h.

were then linked to this core via the Buchwald-Hartwig reaction,[86] **PMO-MeSO$_4$**. Next, the sulfur-containing anion was changed to SCN and iodide using potassium cyanide and potassium iodide yielding a symmetric X-type **PMO** HTM. One of the pyrazine nitrogens in **PMO** was ionized using dimethyl sulfate, yielding the producing **PMO-SCN** and **PMO-I**, respectively. All structures were confirmed using ^{1}H and ^{13}C NMR spectroscopy and high- resolution mass spectra (see details in SI). The synthetic approach of **PMO**-based HTMs gave good product yield overall, that demonstrates the potential for efficient mass manufacturing.

Figure 2a shows the optical properties of **PMO**-based HTMs which the HTMs were dissolved in dichloromethane and measured with UV-vis spectroscopy. The **PMO** absorption profile reveals two strong absorption bands, with maximum absorption at 294 nm and 410 nm. The first strong peak can be attributed to the π–π* local electron transition of the donor units. The second-high energy band have stronger bathochromic shifts, usually coming from intramolecular charge transfer. Like **PMO**, the first strong band for **PMO-MeSO$_4$**, **PMO-SCN**, and **PMO-I** π–π* local electron transition of the donor appears at 290 nm, 290 nm, and 291 nm, respectively. However, the shoulder and second high-energy peaks from **PMO** have split further apart in ionic HTMs, with the latter showing much longer wavelength absorption. Such behavior is understandable, as the ionization of one of the nitrogens in pyrazine might induces a new much higher intramolecular charge transfer due to oxidation. The onset absorption wavelengths (λ_{onset}) of **PMO**, **PMO-MeSO$_4$**, **PMO-SCN**, and **PMO-I** are 472 nm, 699 nm, 700 nm, and 698 nm, respectively. The optical bandgaps (E_g^{opt}) calculated from the equation (E_g^{opt} = 1240/λ_{onset}) for **PMO**, **PMO-MeSO$_4$**, **PMO-SCN**, and **PMO-I** are 2.63 eV, 1.77 eV, 1.77 eV, and 1.78 eV, respectively. Therefore, the HOMO and lowest unoccupied molecular orbital (LUMO) energy levels of **PMO**, **PMO-MeSO$_4$**, **PMO-SCN**, and **PMO-I** HTMs were obtained by using cyclic voltammetry and summrized in Figure 2b and Table 1. The HOMO energy level of **PMO** is -5.33 eV and the LUMO level is determined to be -2.70 eV. However, the Ionization of **PMO** alters the energy levels, and the HOMO and LUMO of **PMO-MeSO$_4$**, **PMO-SCN**, and **PMO-I** are found to be much deeper (HOMO = -5.45 eV, -5.45 eV, and -5.48 eV, respectively; LUMO = -3.68 eV, -3.68 eV, and -3.70 eV, respectively) with **PMO-I** showing the deepest HOMO. Therefore, a higher V_{OC} for **PMO-I**-based devices is expected.

HTMs with high hole mobility help improve device performance in PSCs. In this study, the hole mobilities of the HTMs were evaluated using a space charge limited current (SCLC) technique (Figure 2c) with fluorine-doped tin oxide (FTO)/HTM/Au device structure. The hole mobilities of **PMO**, **PMO-MeSO$_4$**, **PMO-SCN**, and **PMO-I** HTMs are 3.31 × 10^{-4} cm^2 v^{-1} s^{-1}, 3.33 × 10^{-4} cm^2 v^{-1} s^{-1}, 3.54 × 10^{-4} cm^2 v^{-1} s^{-1}, and 3.62 × 10^{-4} cm^2 v^{-1} s^{-1}, respectively, all of which are higher than that of **PEDOT:PSS** (3.16 × 10^{-4} cm^2 v^{-1} s^{-1}). These findings show that the **PMO**-based HTM layers can potentially improve the molecular arrangement at the HTM/perovskite interface with enhancing charge transport properties. The capacity to extract holes is further evaluated using steady-state photoluminescence (PL) and time-resolved photoluminescence (TRPL). Figure 2d shows that the degree of PL quenching occurred in HTMs/perovskites interface in the following order: **PMO-I** > **PMO-SCN** > **PMO-MeSO$_4$** > **PMO** > **PEDOT:PSS** > pristine perovskite, indicating that **PMO-I** has the best hole extraction ability than other **PMO**-based HTM and **PEDOT:PSS**. The TRPL spectra obtained from perovskite films over various HTM layers (Figure S1; Table S1 in Supporting information) also support the obtained PL quenching trend. As a result, the **PMO**-I had shorter initial fast decay (τ_1 = 0.6980 ns) and second slow decay (τ_2 = 2.6811 ns), resulting in a shorter average decay time (τ_{avg} = 1.509 ns). **PEDOT:PSS**, **PMO**, **PMO-MeSO$_4$**, and **PMO-SCN**, on the other hand, have higher initial fast decay (τ_1 = 1.7197 ns, 3.3416 ns, 3.2037 ns, and 1.5049 ns) and second slow decay (τ_2 = 8.3250 ns, 7.3400 ns, 7.4159 ns, and 6.7962 ns), resulting in average decay times of 6.952 ns, 5.349 ns, 4.990 ns, and 3.412 ns, respectively. The data shows that the **PMO-I** extracts holes more efficiently compared to other HTMs.

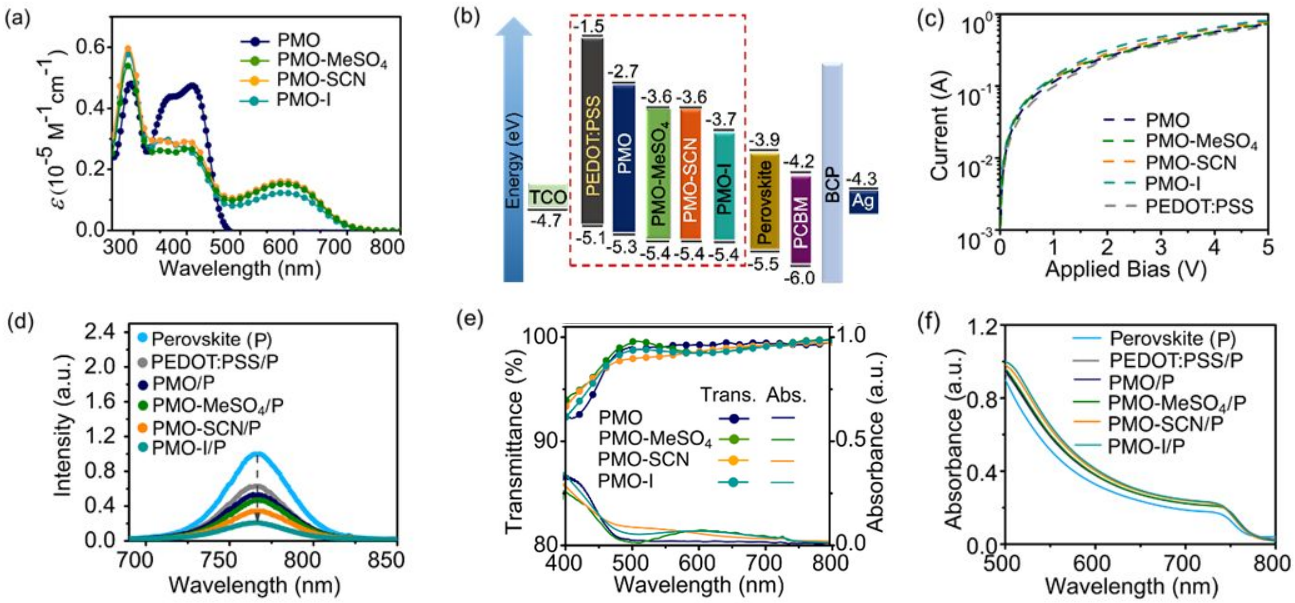

Figure 2. (a) UV-vis absorption measured in a 1×10^{-5} M dichloromethane solution. (b) Energy level diagram of HTMs in this study. (c) SCLC mobilities of devices with the configuration of FTO/HTM/Au. (d) Steady-state PL spectra for perovskites and perovskites/HTM interface. (e) UV-vis absorption and transmittance spectra of different HTM films. (f) UV-vis absorption of perovskite films on FTO and different HTMs.

ARTICLE

Table 1. Optical and electrochemical properties of HTMs.

HTMs	λ_{abs} (nm)[a)]	λ_{onset} (nm)[b)]	E_g^{opt} (eV)[c)]	E_{HOMO} (eV)[d)]	E_{LUMO} (eV)[e)]
PMO	294, 367, 410	472	2.63	-5.33	-2.70
PMO-MeSO$_4$	290, 398, 579	699	1.77	-5.45	-3.68
PMO-SCN	290, 401, 579	700	1.77	-5.45	-3.68
PMO-I	291, 359, 579	698	1.78	-5.48	-3.70

[a)]Measured in a 1×10^{-5} M DCM solution at room temperature; [b)]The onset (λ_{onset}) of absorption; [c)]Energy gap was calculated from the onset: E_g (eV) = 1240/λ; [d)]TBAPF$_6$ (0.1 M) was used as electrolyte in DCM; Potential vs. ferrocene/ferrocenium redox couple; E_{HOMO} = -5.1 - ($E_{onset}^{ox} - E_{onset}^{Fc}$); [e)]$E_{LUMO}$ = $E_{HOMO} + E_g$.

Figure 2e displays the UV-vis absorption and transmittance of **PMO**, **PMO-MeSO$_4$**, **PMO-SCN**, and **PMO-I** films. The spectrum of **PMO** film shows an absorption maximum of 408 nm, while it appears at 401 nm, 399 nm, and 398 nm for **PMO-MeSO$_4$**, **PMO-SCN**, and **PMO-I** films, respectively. The spectra HTM films have a slight blue shift of absorption maxima compared to those of HTM solutions. However, compared to the solution data, spectra of the ionic HTM films display a bluer shift in absorption maxima, indicating more intermolecular interactions in the solid state compared to **PMO**. The optical transparency spectra of all HTMs (**PMO**, **PMO-MeSO$_4$**, **PMO-SCN**, and **PMO-I**) are shown in Figure 2e. All the HTMs have a similar transmittance range of 450-800 nm, and the transmittance values remain above 95%. These findings indicate that the perovskite layer coated on top of these HTMs will harvest enough light. The UV-vis spectra of perovskite films deposited on **PMO**, **PMO-MeSO$_4$**, **PMO-SCN**, and **PMO-I** (Figure 2f) also support this conclusion. Additionally, these studies include a standard **PEDOT:PSS** HTM as a comparison. The FTO/HTMs/perovskite films of all the HTMs in this study exhibit similar absorption trends in the region of 500-800 nm. The UV-vis absorbance patterns observed is **PMO-I** > **PMO-SCN** > **PMO-MeSO$_4$** > **PMO** > **PEDOT:PSS**.

The morphology and surface wettability of the HTM employed in inverted PSCs determine the crystal quality of perovskite films. The scanning electron microscopy (SEM) characterizations (Figure 3) show films with smooth surfaces with less pinholes. The films deposited on **PMO-MeSO$_4$**, **PMO-SCN**, and **PMO-I** has more aligned grain boundaries and denser grains than the film deposited on **PMO** and **PEDOT:PSS** (Figure S2), indicating formations of high-quality perovskite films. The contact angles of water droplets on the surface of **PEDOT:PSS**, **PMO**, **PMO-MeSO$_4$**, **PMO-SCN**, and **PMO-I** were also measured to determine their surface wettability (inset in Figure 3). **PEDOT:PSS**, **PMO**, **PMO-MeSO$_4$**, **PMO-SCN**, and **PMO-I** have contact angles of 13.26^o, 71.10^o, 61.31^o, 65.34^o, and 64.34^o, respectively. Salt form HTMs exhibits a slightly lower contact angle than **PMO** due to the ionic nature that induces the hydrophilic character in the film. Nevertheless, all HTMs have higher contact angles than **PEDOT:PSS** (inset in Figure S2). Figure S3a shows the X-ray diffraction (XRD) patterns of perovskite films on **PEDOT:PSS**, **PMO**, **PMO-MeSO$_4$**, **PMO-SCN**, and **PMO-I**. These films coated on HTMs have similar diffraction peaks, about 14.28^0 and 28.45^0, with **PMO-I** peaks slightly more substantial than others (Figure S3b), indicating film formation with better homogeneity and crystallinity, which may help to reduce recombination losses and improve carrier collections.

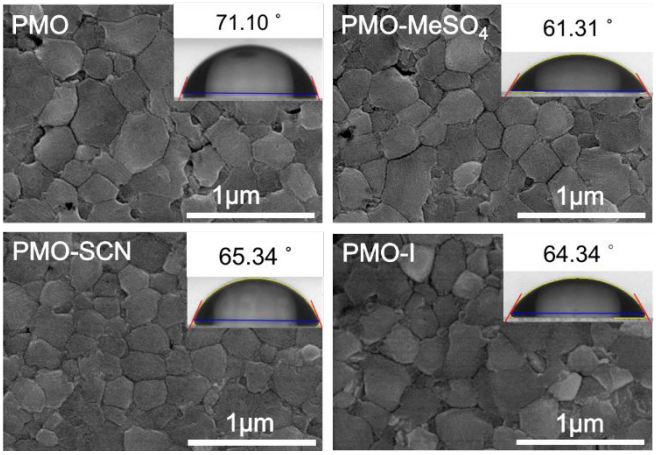

Figure 3. SEM images (Top view) with inset water contact angles of **PMO**, **PMO-MeSO$_4$**, **PMO-SCN**, and **PMO-I**.

Using the inverted device configuration of FTO/HTM/triple-cation lead mixed-halide perovskites/[6,6]-phenyl-C$_{61}$-butyric acid methyl ester (PCBM)/ bathocuproine(BCP)/Ag, the PSCs were fabricated by incorporating **PMO**, **PMO-MeSO$_4$**, **PMO-SCN**, and **PMO-I** layer as HTMs. The current density-voltage (*J-V*) characteristic curves of the devices using these HTMs are shown in Figure 4a and their corresponding photovoltaic characteristics are summarized in Table 2. The device based on **PMO** HTM with forward scan direction exhibited PCE = 18.29% with V_{OC} =1.02 V, J_{SC} = 22.37 mA cm^{-2}, and a fill factor, *FF* = 80.12%. In addition, the device with reverse scan direction exhibited higher PCE of 18.75% with V_{OC}, $J_{SC,}$ and *FF* of 1.02 V, 22.82 mA cm^{-2}, and 80.12%, respectively. When we introduce the ionic character into the **PMO**-based HTMs, which lead to an increase in V_{OC} and J_{SC} values. For the device based on **PMO-MeSO$_4$** HTM exhibited PCE of 18.85% with V_{OC}, $J_{SC,}$ and *FF* of 1.04 V, 22.49 mA cm^{-2}, and 80.61%, respectively, with forward scan, and PCE of 19.33% with V_{OC}, $J_{SC,}$ and *FF* of 1.04 V, 23.01 mA cm^{-2}, and 80.67%, respectively, with reverse scan. Moreover, substituting CH_3SO_4 with the SCN anion in **PMO** structure produced further enhancement in efficiency: the device based on **PMO-SCN** displays PCE = 19.30% with V_{OC}, $J_{SC,}$ and *FF* of 1.07 V, 22.34 mA cm^{-2}, and 80.58%, respectively, with a forward scan, and PCE = 19.53% with V_{OC}, $J_{SC,}$ and *FF* of 1.07 V, 22.35 mA cm^{-2}, and 81.81%, respectively, with a reverse scan. Furthermore, by substituting SCN with the iodide anion, the efficiency was increased even further: the device based on **PMO-I** displays PCE = 20.27% with V_{OC}, $J_{SC,}$ and *FF* of 1.10 V, 22.88 mA cm^{-2}, and 80.19, respectively, with a forward scan, and PCE = 20.46% with V_{OC}, $J_{SC,}$ and *FF* of 1.10 V, 22.88 mA cm^{-2}, and 80.96%, respectively,

ARTICLE

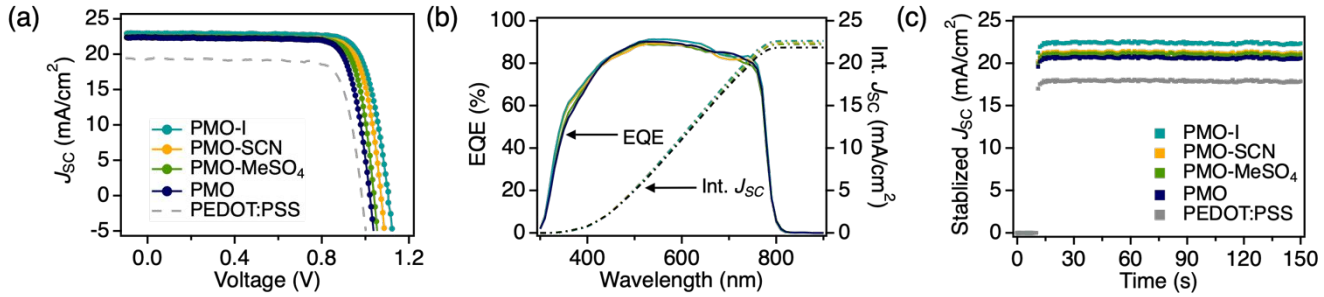

Figure 4. (a) *J-V* characteristic curves and (b) EQE spectra (solid line) with integrated J_{SC} (dashed line) of the PSCs with **PMO-I** (dark cyan), **PMO-SCN** (orange), **PMO-MeSO$_4$** (olive), **PMO** (royal blue). (c) Steady-state photocurrent output of PSCs based on various HTMs measured at the maximum power point in this study.

with a reverse scan. The champion performance of **PMO-I**-based PSCs is mainly attribute to a 0.08 V increase in V_{OC} compared to that of the parent **PMO** HTM. The higher V_{OC} indicates that **PMO-I** devices have better energy level alignment with the perovskite valance band, which could be explained by increased electron negativity in the pyrazine core caused by ionization. The obtained higher J_{SC} results from fewer defects and better crystallinity in the perovskite layer, which leads to less non-radiative recombination. Ionic HTMs in this study has higher J_{SC} than the non-ionic HTM, indicating that the salt form assists the formation of the perovskite layer with fewer defects and higher crystallinity, as evidenced by SEM and UV film tests. The forward and reverse bias scans of **PEDOT:PSS** HTM are further used for comparison yielded PCE, V_{OC}, J_{SC}, and *FF* values of 14.74%, 0.98 V, 18.56 mA cm^{-2}, 80.79 and 14.68%, 0.98 V, 18.70 mA cm^{-2}, 79.86, respectively (Figure S4a).

The external quantum efficiency (EQE) spectra of devices with the respective HTMs, namely **PMO-I** (dark cyan), **PMO-SCN** (orange), **PMO-MeSO$_4$** (olive), **PMO** (royal blue), are shown in Figure 4b. All these devices have broad absorption characteristics that covered the visible spectra range between 400 to 800 nm. At 560 nm, the maximum EQE value for HTM **PMO**, **PMO-MeSO$_4$**, **PMO-SCN**, and **PMO-I** is above 88.73%. The EQE curve for the PSC with **PEDOT:PSS**, on the other hand, obtained a maximum EQE value of 76% at 480 nm (Figure S4). The integrated current densities calculated from EQE spectra for **PEDOT:PSS** (Figure S4) and **PMO**, **PMO-MeSO$_4$**, **PMO-SCN**, and **PMO-I** (Figure 4b) are 16.89 mA cm^{-2}, 21.85 mA cm^{-2}, 22.25 mA cm^{-2}, 22.44 mA cm^{-2}, and 22.63 mA cm^{-2}, respectively, and the results are in good agreement with the experimental J_{SC} data. Further, **PMO**, **PMO-MeSO$_4$**, **PMO-SCN**, **PMO-I**-based and **PEDOT:PSS** PSCs were tested for stability with the findings and summarized in Figure 4c. A stabilized J_{SC} of 21.20 mA cm^{-2}, 21.63 mA cm^{-2}, 21.86 mA cm^{-2}, and 22.29 mA cm^{-2} and 17.96 mA cm^{-2} at maximum power point of 0.85 V, 0.92 V, 0.94 V, 0.95 V and 0.98 V for **PMO**, **PMO-MeSO$_4$**, **PMO-SCN**, **PMO-I** and **PEDOT:PSS**-based PSCs, respectively, which show the stable output over 150 s and indicate that these devices work adequately under operating conditions.

Table 2. The best photovoltaic efficiency performance of the inverted PSCs with forward scan and based on **PEDOT:PSS**, **PMO**, **PMO-MeSO$_4$**, **PMO-SCN**, and **PMO-I**.

HTMs	V_{OC} (V)	J_{SC} (mA/cm^2)	*FF*	PCE (%)	Hole mobility (cm^2 v^{-1} s^{-1})
PEDOT:PSS	0.98	18.70	79.86	14.68	3.16×10^{-4}
PMO	1.02	22.82	80.12	18.75	3.31×10^{-4}
PMO-MeSO$_4$	1.04	23.01	80.67	19.33	3.33×10^{-4}
PMO-SCN	1.07	22.35	81.81	19.53	3.54×10^{-4}
PMO-I	1.10	22.88	80.96	20.46	3.62×10^{-4}

To rationalize enhanced PCE of PSCs with modified **PMO**-based HTMs, we perform detailed atomistic first-principal simulations using Density Functional Theory (DFT) framework as briefly outlined in Supplemental information. Initially, we model the thermodynamically stable and experimentally observed $MAPbI_3$ (001) surface that has MAI termination.[87] The optimized slab geometry of $MAPbI_3$ that we simulate using dispersion-corrected DFT approach depicts minor surface relaxations and maintains overall octahedral connectivity as also reported previously (Figure S5a).[88-90] The electronic structure calculations show that the MAI-terminated (001) surface formation does not incorporate any defect state inside the bandgap, revealing defect-tolerance of $MAPbI_3$ towards these surface formations (Figure S5b). However, such a clean defect-free surface is not realistic under ambient experimental conditions. To model a more realistic surface, we further introduce a neutral iodine vacancy (V_I), which has been identified as the most dominant point defect in the halide perovskites due to its low formation energy (Figure 5a).[91, 92] The V_I does not impact the overall geometry of the surface or the remaining bulk of $MAPbI_3$. However, surface V_I influences the electronic structure by introducing a shallow defect state that appears just below the conduction band level (Figure 5b). The charge density of the associated defect state exhibits a prominent charge localization in the $6p_z$ orbitals of undercoordinated and subsurface Pb atoms (Figure 5c). Even though a native V_I defect only produces a shallow trap, structural change in the defect

ARTICLE

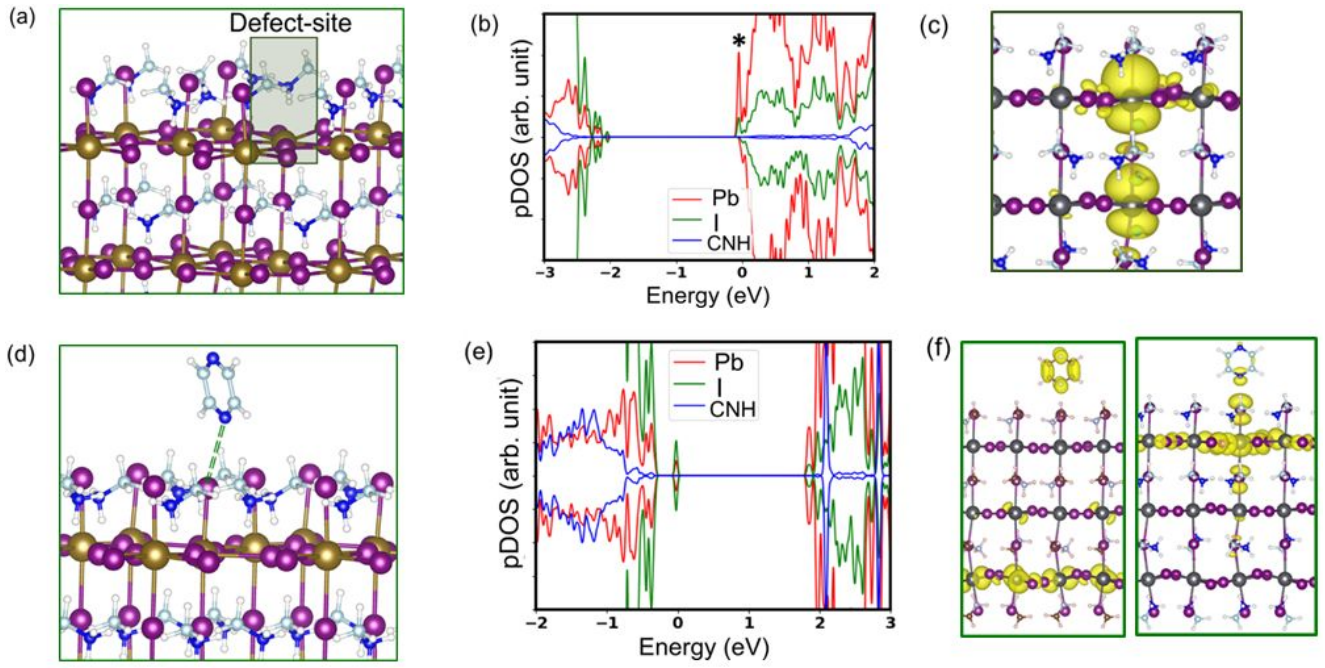

Figure 5. The optimized structures and electronic properties of defective and passivated iodide perovskites. (a) The optimized geometry and (b) partial density of states (pDOS) of neutral V_I included on (001) surface of $MAPbI_3$. (c) The charge density of the defect state is marked as "*" in the pDOS plot (b). The defect state is dominantly localized on the undercoordinated Pb atom on the surface. (d) The optimized structure and (e) pDOS of **PMO-I** treated defective $MAPbI_3$. The dashed green line in (d) represents the elongated distance between the passivating I ion and N atom of the pyrazine ring. The defect state gets removed as iodide from **PMO-I** passivates the defect site on the surface. (f) The charge density of the CBM (left panel) and VBM (right panel) of $MAPbI_3$ with **PMO-I**. The band edge states show considerable delocalization of charge with V_I passivation. Key: lead (brown), iodine (pink), carbon (light blue), hydrogen (white), nitrogen (blue).

geometry during post-processing and high density can give rise to deep trap levels that act as nonradiative recombination centers for charge carriers.[92-94] These V_I sites can also accelerate the surface degradation of $MAPbI_3$.

To simulate the effect of ionic HTMs on defect passivation, we next model the V_I containing $MAPbI_3$ surface in the presence of **PMO-I** or **PMO-SCN** molecules (Figure 5d and S6a). To make such computation feasible, we consider only the pyrazine ring and the ionic group (I or SCN) on the surface. The geometry optimization reveals that the I and SCN groups dissociate from the pyrazine ring and form a covalent bond with an undercoordinated Pb atom, passivating the V_I site (Figure 5d and Figure S6a). The optimized perovskite (001) surface with **PMO-I** in particular, shows efficient passivation as the iodide atom occupies the defect site, completely healing the defect. In contrast, the small-sized N of SCN binds to the defective Pb atom, distorting the local geometry to some extent. Thus, over time and under special conditions, the **PMO-SCN** coverage can have less efficient defect passivation compared to **PMO-I**. Modeling such rare events needs a separate elaborate study and has not been considered presently. Note that, the dissociated pyrazine unit from passivating layer does not bind to the $MAPbI_3$ (001) surface to any considerable degree. In Figure 5e and Figure S6b, the partial density of states (pDOS) of passivated $MAPbI_3$ depicts that passivating I and SCN groups effectively removes the shallow trap state and recovers the pristine band gap. The charge densities of the valence band maximum and conduction band minimum in these passivated systems show considerable charge delocalization, indicating mostly removed influences of V_I on the electronic properties of $MAPbI_3$ (Figure 5f and S6c-d). Thus, our computational simulations unambiguously demonstrate that the ionic entities from the **PMO** layer efficiently passivate the surface V_I defects, reducing the density of interfacial trap states at the perovskite/HTL interface. Such modifications in defect properties facilitate enhancement of the PCE of **PMO-I** and **PMO-SCN**-passivated halide perovskites.

Experimental

Materials: Chemical reagents used were purchased from Aldrich, Alfa and TCI Chemical Co. and used as received unless otherwise noted. Reactions solvents (CH_2Cl_2, DMF, and THF) were dried using VAC purifier (VAC 103991, Vacuum Atmospheres). Silica gel (Scharlau 60, 230-240 mesh) were utilized for flash chromatography. Aluminum coated Merck Kieselgel 60 F254 plates were used to monitor the reaction progresses under I_2 or UV light. Moisture sensitive reactions were performed using argon atmosphere. Bruker

Avance 500 MHz spectrometer was used to record ^{1}H and ^{13}C NMR spectra of all the intermediates and final compounds. Multiplicities were reported as: singlet = s, doublet = d, triplet = t, quartet = q, pentet = p, multiplet = m, broad = b. Chemical shifts (δ) and coupling constants (J) are denoted with ppm and Hz, respectively. Bruker Daltonics flex Analysis spectrometer was used to record mass spectra matrix assisted Laser desorption ionization (coupled to a Time-of-Flight analyzer) experiments (MALDI-TOF). CHI 627C electrochemical setup was used to perform Cyclic voltammetry experiments. the setup is made up of single-compartment three-electrode cell, the working electrode (glassy carbon electrode), a reference electrode ($Ag/AgNO_3$ in acetonitrile), a counter-electrode (Pt wire), and supporting electrolyte (0.1 M tetrabutylammonium hexafluorophosphate). Cyclic voltammograms of HTMs used in this study were recorded using 50 mVs^{-1} scan rates. For calibration, ferrocene was added as the internal reference. Shimadzu UV3600 UV-vis-NIR spectrophotometer was used to analyze the optical properties in the solutions whereas the UV-Vis films were recorded on a JASCO V-730 spectrophotometer. Scanning electron microscopy (Hitachi SU4800) and X-ray diffraction (BRUKER ECO D8 series) technic were used to study the morphology of the perovskite films. Time resolved PL spectra were measured using a Spectrofluorometer (FS5, Edinburgh instruments) and the PL excitation was at λ = 405 nm. The contact angle measurement were test with Phoenix 300, Surface Electro Optics (SEO) Co., Ltd with de-ionize water as solvent.

Synthetic Procedures:

Synthesis of **2,3,5,6-Tetrakis(4-bromophenyl)pyrazine (2):** Synthesis of 2,3,5,6-Tetrakis(4-bromophenyl)pyrazine is performed according to literature.[95]

Synthesis of **PMO:** A solution of the compound **2** (0.30 g, 0.43 mmol), bis(4-methoxyphenyl)amine (0.43 g, 1.9 mmol) with $Pd(OAc)_2$ (3.0 mg, 0.013 mmol), P(*t*-Bu)$_3$ (0.80 mg, 0.0043 mmol) and NaO-*t*-Bu (0.20 g, 2.1 mmol) in 4 mL of toluene was refluxed for 12 h under nitrogen atmosphere. The solvent was removed in vacuo, and the residue was purified on a gradient column chromatograph (silica gel) using (THF/hexane = 20%~50%) as eluent, and then recrystallized with DCM/methanol to yield yellow solid **PMO** (0.50 g, 90%). mp 306.0-308.0℃. ^{1}H NMR (500 MHz, $CDCl_3$, 298K) δ 7.49 (d, J = 8.5 Hz, 8H), 7.07 (d, J = 9.0 Hz, 16H), 6.83 (d, J = 9.0 Hz, 24H), 3.80 (s, 24H). ^{13}C NMR (125 MHz, $CDCl_3$, 298K) δ 156.1 148.9, 146.4, 140.7, 130.7, 130.5, 127.0, 119.4, 114.8, 55.6. HRMS (MALDI-TOF, m/z): calculated for = $C_{84}H_{72}N_6O_8$, $[M]^+$ = 1292.5406, found: 1292.5406.

Synthesis of **PMO-MeSO$_4$**: In a 50 mL round-bottomed flask, **PMO** (0.30 g, 0.23 mmol), dimethyl sulfate (3.9 g, 31 mmol) were mixed in dioxane (12 mL), and the resulting mixture was refluxed at 120 °C for 12 hours. After cooling to room temperature, the reaction mixture was extracted with CH_2Cl_2, washed with brine several times, and the organic layer was dried with anhydrous magnesium sulfate. The solvent was evaporated under vacuum, and the residue was purified by gradient column chromatography using THF/methanol = 5%~10%, followed by recrystallization with DCM/hexane to obtain a black solid **PMO-MeSO$_4$** (0.22 g, 67%). mp 162.0-164.0℃. ^{1}H NMR (500 MHz, $CDCl_3$, 298K) δ 7.42 (d, J = 9.0 Hz, 4H), 7.22 (d, J = 9.0 Hz, 4H), 7.07 (t, J = 9.5 Hz, 16H), 6.91 (d, J = 8.5 Hz, 4H), 6.87 (d, J = 7.0 Hz, 8H), 6.85 (d, J = 7.0 Hz, 8H), 6.74 (d, J = 9.0 Hz, 4H), 4.07 (s, 3H), 3.81 (s, 12H), 3.80 (s, 12H), 3.48 (s, 3H). ^{13}C NMR (125 MHz, $CDCl_3$, 298K) δ 157.0, 156.7, 150.9, 150.1, 144.0, 139.9, 139.4, 131.7, 131.1, 127.7, 127.4, 127.3, 120.5, 118.57, 118.2, 115.1, 114.9, 55.6, 55.6, 54.2, 47.4. HRMS (MALDI-TOF, m/z): calculated for = $C_{85}H_{75}N_6O_8^+$, $[M\text{-}CH_3SO_4]^+$ = 1307.5641, found: 1307.5641.

Synthesis of **PMO-SCN**: In a 25 mL round-bottomed flask, **PMO** (0.30 g, 0.23 mmol), dimethyl sulfate (3.9 g, 31 mmol) were mixed in dioxane (12 mL), and the resulting mixture was refluxed at 120 °C for 12 hours. After cooling to room temperature, the solvent was evaporated under vacuum, and the residue was in dissolved with a small amount of methanol, a saturated aqueous KSCN solution was added, and the mixture was stirred at room temperature for 3 hours. The reaction mixture was extracted with CH_2Cl_2, washed with water, and the solvent was evaporated under vacuum. The residue was purified by gradient column chromatography using THF/hexane = 20%~50%, followed by recrystallization with DCM/hexane to get a black solid **PMO-SCN** (0.24 g, 76%). mp 158.0-160.0℃. ^{1}H NMR (500 MHz, $CDCl_3$, 298K) δ 7.39 (d, J = 8.7 Hz, 4H), 7.22 (d, J = 8.9 Hz, 4H), 7.10 (d, J = 8.9 Hz, 8H), 7.06 (d, J = 8.9 Hz, 8H), 6.94 (d, J = 8.7 Hz, 4H), 6.86 (t, J = 9.3 Hz, 16H), 6.74 (d, J = 8.9 Hz, 4H), 4.14 (s, 3H), 3.80 (s, 12H), 3.79 (s, 12H). ^{13}C NMR (125 MHz, $CDCl_3$, 298K) δ 157.1, 157.0, 156.7, 151.0, 150.2, 143.8, 139.8, 139.3, 131.6, 131.2, 127.7, 127.4, 127.0, 120.2, 118.5, 118.1, 115.1, 114.9, 55.6, 55.6, 47.6. HRMS (MALDI-TOF, m/z): calculated for = $C_{85}H_{75}N_6O_8^+$, $[M\text{-}SCN]^+$ = 1307.5641, found : 1307.5641.

Synthesis of **PMO-I**: **PMO-I** was synthesized using the similar method as **PMO-SCN**, with the following reagent parameters: **PMO** (0.20 g, 0.15 mmol), dimethyl sulfate (2.6 g, 21 mmol), dioxane (8 mL), and saturated aqueous KI solution. **PMO-I** was obtained as black solid (0.17 g, 77 %). mp 164.0-166.0℃. ^{1}H NMR (500 MHz, $CDCl_3$, 298K) δ 7.56 (d, J = 9.0 Hz, 4H), 7.23 (d, J = 8.5 Hz, 4H), 7.09 (d, J = 9.0 Hz, 8H), 7.06 (d, J = 9.0 Hz, 8H), 6.91 (d, J = 8.5 Hz, 4H), 6.86 (t, J = 9.0 Hz, 16H), 6.74 (d, J = 8.5 Hz, 4H), 4.10 (s, 3H), 3.81 (s, 12H), 3.80 (s, 12H). ^{13}C NMR (125 MHz, $CDCl_3$, 298K) δ 157.1, 157.0, 156.7, 151.0, 150.1, 143.6, 139.90, 139.3, 132.4, 131.2, 127.7, 127.4, 127.2, 120.2, 118.4, 118.2, 115.1, 114.9, 55.6, 55.6, 47.9. HRMS (MALDI-TOF, m/z): calculated for = $C_{85}H_{75}N_6O_8^+$, $[M\text{-}I]^+$ = 1307.5641, found : 1307.5641.

Device fabrication:

The fluoride-dope tin oxide (FTO) conducting glass substrates were cleaned in an ultrasonic cleaner for 15 minutes each with detergent, deionized water, acetone, and isopropanol. The cleaned glasses were then treated with ultraviolet ozone (UV-ozone) for 15 min and transferred to a glovebox. Inside the N_2-filled glovebox, anhydrous chlorobenzene solvents were used to make HTM solutions (conc. 2 mg/mL). These solutions were then spin-coated on FTO substrates at 4000 rpm for 30 seconds before being annealed at 100 °C for 10 minutes. The **PEDOT:PSS** film was prepared by first filtering its stock solution via a 0.22 m PVDF filter and then spin-coated on the FTO at 5000 rpm for 30 seconds, followed by heating at 120 °C for 20 minutes. The film was then transferred to the glovebox. The solution of ($Cs_{0.05}FA_{0.78}MA_{0.17}PbI_{2.53}Br_{0.47}$, FAMACs) mixed-cation mixed-halide perovskites used was prepared inside the N_2-filled glove box by mixing MAI (34 mg), FAI (145 mg), CsI (16.8 mg), PbI_2 (510 mg) and $PbBr_2$ (71.3 mg) in 1 mL of DMF:DMSO (4:1) mix solvent and stirring at 70 °C. Antisolvent process was used to get the

final perovskite thin films. First, the prepared perovskite solution (85 µL) was spin-coated in two steps at 1000 and 6000 rpm for 10 and 20 s, respectively. Then, at the last 5 s of the procedure, 200 µL of chlorobenzene was dropped on the perovskite layer, which gives transparent brown perovskite film. The film turned darker after annealing at 100 °C for 1 hour in a nitrogen-filled glove box. The film was cooled and 50 µL of [6,6]-phenyl-C_{61}-butyric acid methyl ester (PCBM, 20 mg mL^{-1} in chlorobenzene) filtered through a 0.45 µm PTFE was spin-coated at 1000 rpm for 60 s. The film was then allowed to stand for 30 min to dry the solvent. On the top of this PCBM layer, a ~3 nm thick finishing bathocuproine (BCP) layer was vapor-deposited. Finally, a 100 nm thick Ag electrode with a defined area of 0.5 cm^2 with a shadow mask was deposited by thermal evaporation in a vacuum deposition chamber at 10^{-7} torr pressure.

Device characterizations:

Keithley 2400 measurement source units was used to measure the *J-V* characteristics, with the devices maintained at room temperature in glovebox. The photovoltaic testing was measured under a calibrated solar simulator (Class 3A, SS-F5-3A, Enli Technology) at 100 mW cm^{-2} with defined shadow mask area of 0.24 cm^2. A standard photovoltaic reference cell was used to calibrate the light intensity (SRC-2020 series, Enli Technology). The light intensity test were changed through the software (IVS-KA6000) from Enli Technology. Enli Technology's QE-R Model was used to measure the EQE spectrum. The electrochemical impedance spectroscopy measurements were performed using Metrohm Autolab PGSTAT 302N. A Xenon lamp at 100 mW cm^{-2} with an air mass AM1.5G spectrum filter was used as the light source. A small AC perturbation voltage of 15 mV was applied to the devices, and the different output current was measured throughout a frequency range of 1 MHz^{-1} Hz.

Computational Methods:

We perform all the computational simulations using density functional theory (DFT) as employed in the Vienna Ab Initio Simulation Package (VASP).[96,97] The projected augmented wave (PAW) method with a plane-wave basis set of 400 eV are considered for all calculations.[98] The considered exchange and correlation interactions are semi-local generalized gradient approximation (GGA) with the Perdew-Burke- Ernzerhof functional (PBE).[99] To effectively sample the Brillouin zone a 4×4×1 and 8×8×1 Γ-centered k-point meshes are used during structural optimization and self-consistent field calculations, respectively. To incorporate dispersion corrections, DFT-D3 method as prescribed by Grimme is used for all simulations.[100] To model the (001) surface of $MAPbI_3$ a 2×2 surface model of room-temperature tetragonal $MAPbI_3$ was considered (total 360 atoms in halide perovskite slab). We model the **PMO** with only pyrazine molecule to reduce the computational cost but does not miss out any key insights.

Conclusions

In conclusion, we demonstrate that ionizing HTMs is a viable method for creating additive-free hole-transporting materials capable of producing high-performing PSCs. **PMO** and **PMO-I** HTMs are obtained through inexpensive and straightforward synthesis and may be very appealing for producing low-cost PSCs, thereby addressing one of the major concerns for near-term commercialization. When compared to the non-ionized counterpart, ionization affects the absorption and emission properties, energy levels, hole mobility, and hydrophilicity of HTMs. The ionic HTM **PMO-I** has well-matched energy levels with the perovskite layer, resulting in an improved charge transfer and electron blocking capabilities. Additionally, ionization increases hydrophilicity and helps forming large-grained perovskite layer, which results in a higher short-circuit current density and, consequently, better PCE. The in-depth atomistic modeling study further points out that the ionic entities such as iodide and SCN can efficiently passivate the dominant surface halogen vacancies, which reduces the density of charge trapping defect states. We believe that our work paves the way for the development of next generation ionized HTMs to improve PSCs performance while maintaining their operational stability.

Conflicts of interest

There are no conflicts to declare.

Acknowledgements

Y.S.T., C.-H.L., C.-C.S., C.-S.C., Y.-C. H, N.-W.L., X.-R.L., and W.-R.L. thank the Ministry of Science and Technology, ROC, for financial support (grants NSTC 112-2221-E-027 -024 -MY2, NSTC 112-2221-E-027-027, and MOST 111-2113-M-008-009). This work was performed, in part, at the Center for Integrated Nanotechnologies, an Office of Science User Facility operated for the U.S. Department of Energy (DOE) Office of Science by Los Alamos National Laboratory (LANL) (Contract 89233218CNA000001).

Author Contributions

Y.S.T. and C.-H.L. synthesized the hole-transporting materials. S.-C.C., Y.-C.H., Y.S.T. and H.T. performed device fabrication and cell data analysis. C.-H.L. and X.-R.L. completed material characterizations and photochemical experiments. S.-C.C., Y.-C.H., and N.-W.L. did photophysical experiments and data analysis. D.G. performed theoretical calculations. Y.S.T., H.T., C.S., and W.-R.L. drafted, revised, and finalized the manuscript. S.T. and W. N. revised the manuscript. C.S., Y.S.T., and W.-R.L. conceptualized the HTM design principles, carried out project administration and validation, applied and acquired the resources and funding's. All authors reviewed the manuscript and have given approval to the final version of the manuscript.

References

1. G. Kim, H. Min, K. S. Lee, D. Y. Lee, S. M. Yoon and S. I. Seok, *Science*, 2020, **370**, 108-112.
2. H. Min, D. Y. Lee, J. Kim, G. Kim, K. S. Lee, J. Kim, M. J. Paik, Y. K. Kim, K. S. Kim, M. G. Kim, T. J. Shin and S. Il Seok, *Nature*, 2021, **598**, 444-450.

3. J. J. Yoo, G. Seo, M. R. Chua, T. G. Park, Y. Lu, F. Rotermund, Y.-K. Kim, C. S. Moon, N. J. Jeon, J.-P. Correa-Baena, V. Bulović, S. S. Shin, M. G. Bawendi and J. Seo, *Nature*, 2021, **590**, 587-593.
4. Z. Li, B. Li, X. Wu, S. A. Sheppard, S. Zhang, D. Gao, N. J. Long and Z. Zhu, *Science*, 2022, **376**, 416-420.
5. *National Renewable Energy Laboratory*, "Best research-cell efficiency chart" (2022), www.nrel.gov/pv/cell-efficiency.html.
6. L. Etgar, P. Gao, Z. Xue, Q. Peng, A. K. Chandiran, B. Liu, M. K. Nazeeruddin and M. Grätzel, *J. Am. Chem. Soc.*, 2012, **134**, 17396-17399.
7. M. M. Lee, J. Teuscher, T. Miyasaka, T. N. Murakami and H. J. Snaith, *Science*, 2012, **338**, 643-647.
8. H.-S. Kim, C.-R. Lee, J.-H. Im, K.-B. Lee, T. Moehl, A. Marchioro, S.-J. Moon, R. Humphry-Baker, J.-H. Yum, J. E. Moser, M. Grätzel and N.-G. Park, *Sci Rep*, 2012, **2**, 591.
9. S. D. Stranks, G. E. Eperon, G. Grancini, C. Menelaou, M. J. P. Alcocer, T. Leijtens, L. M. Herz, A. Petrozza and H. J. Snaith, *Science*, 2013, **342**, 341-344.
10. G. Xing, N. Mathews, S. Sun, S. S. Lim, Y. M. Lam, M. Grätzel, S. Mhaisalkar and T. C. Sum, *Science*, 2013, **342**, 344-347.
11. M. Saliba, T. Matsui, J.-Y. Seo, K. Domanski, J.-P. Correa-Baena, M. K. Nazeeruddin, S. M. Zakeeruddin, W. Tress, A. Abate, A. Hagfeldt and M. Grätzel, *Energy Environ. Sci.*, 2016, **9**, 1989-1997.
12. J. Burschka, N. Pellet, S.-J. Moon, R. Humphry-Baker, P. Gao, M. K. Nazeeruddin and M. Grätzel, *Nature*, 2013, **499**, 316-319.
13. G. E. Eperon, S. D. Stranks, C. Menelaou, M. B. Johnston, L. M. Herz and H. J. Snaith, *Energy Environ. Sci.*, 2014, **7**, 982-988.
14. Y. Li, L. Meng, Y. Yang, G. Xu, Z. Hong, Q. Chen, J. You, G. Li, Y. Yang and Y. Li, *Nat. Commun.*, 2016, **7**, 10214.
15. Y. Zhang, A. Kirs, F. Ambroz, C.-T. Lin, A. S. R. Bati, I. P. Parkin, J. G. Shapter, M. Batmunkh and T. J. Macdonald, *Small Methods*, 2021, **5**, 2000744.
16. M. Cai, Y. Wu, H. Chen, X. Yang, Y. Qiang and L. Han, *Adv. Sci.*, 2017, **4**, 1600269.
17. T. Wu, Z. Qin, Y. Wang, Y. Wu, W. Chen, S. Zhang, M. Cai, S. Dai, J. Zhang, J. Liu, Z. Zhou, X. Liu, H. Segawa, H. Tan, Q. Tang, J. Fang, Y. Li, L. Ding, Z. Ning, Y. Qi, Y. Zhang and L. Han, *Nanomicro Lett.*, 2021, **13**, 152-152.
18. P. Murugan, T. Hu, X. Hu and Y. Chen, *Adv. Optical Mater.*, 2021, **9**, 2100390.
19. J. Ling, P. K. K. Kizhakkedath, T. M. Watson, I. Mora-Seró, L. Schmidt-Mende, T. M. Brown and R. Jose, *Sol. RRL*, 2021, **5**, 2100401.
20. X. Lin, D. Cui, X. Luo, C. Zhang, Q. Han, Y. Wang and L. Han, *Energy Environ. Sci.*, 2020, **13**, 3823-3847.
21. M. Degani, Q. An, M. Albaladejo-Siguan, Y. J. Hofstetter, C. Cho, F. Paulus, G. Grancini and Y. Vaynzof, *Science Adv.*, 2021, **7**, eabj7930.
22. H. D. Pham, T. C.-J. Yang, S. M. Jain, G. J. Wilson and P. Sonar, *Adv. Energy Mater.*, 2020, **10**, 1903326.
23. G.-W. Kim, H. Choi, M. Kim, J. Lee, S. Y. Son and T. Park, *Adv. Energy Mater.*, 2020, **10**, 1903403.
24. S. Yang, W. Ma, Z. Zhang, J. Zhu, Y. Liu, H. Zhang and Y. Mao, *Solar Energy*, 2021, **230**, 485-491.
25. G. M. Arumugam, S. K. Karunakaran, C. Liu, C. Zhang, F. Guo, S. Wu and Y. Mai, *Nano Select*, 2021, **2**, 1081-1116.
26. A. Kumar and S. Singh, *J. Electron. Mater.*, 2020, **49**, 5840-5881.
27. K. Jiang, J. Wang, F. Wu, Q. Xue, Q. Yao, J. Zhang, Y. Chen, G. Zhang, Z. Zhu, H. Yan, L. Zhu and H.-L. Yip, *Adv. Mater.*, 2020, **32**, 1908011.
28. W. Chen, Y. Zhou, L. Wang, Y. Wu, B. Tu, B. Yu, F. Liu, H.-W. Tam, G. Wang, A. B. Djurišić, L. Huang and Z. He, *Adv. Mater.*, 2018, **30**, 1800515.
29. S. Ye, H. Rao, W. Yan, Y. Li, W. Sun, H. Peng, Z. Liu, Z. Bian, Y. Li and C. Huang, *Adv. Mater.*, 2016, **28**, 9648-9654.
30. W. Sun, S. Ye, H. Rao, Y. Li, Z. Liu, L. Xiao, Z. Chen, Z. Bian and C. Huang, *Nanoscale*, 2016, **8**, 15954-15960.
31. V. E. Madhavan, I. Zimmermann, C. Roldán-Carmona, G. Grancini, M. Buffiere, A. Belaidi and M. K. Nazeeruddin, *ACS Energy Letters*, 2016, **1**, 1112-1117.
32. W. Chen, Y. Wu, Y. Yue, J. Liu, W. Zhang, X. Yang, H. Chen, E. Bi, I. Ashraful, M. Grätzel and L. Han, *Science*, 2015, **350**, 944-948.
33. W. Chen, Y. Wu, J. Fan, A. B. Djurišić, F. Liu, H. W. Tam, A. Ng, C. Surya, W. K. Chan, D. Wang and Z.-B. He, *Adv. Energy Mater.*, 2018, **8**, 1703519.
34. J. Príncipe, V. C. M. Duarte and L. Andrade, *Energy Technol.*, 2022, **10**, 2100952.
35. X. Yin, Z. Song, Z. Li and W. Tang, *Energy Environ. Sci.*, 2020, **13**, 4057-4086.
36. P. Mahajan, B. Padha, S. Verma, V. Gupta, R. Datt, W. C. Tsoi, S. Satapathi and S. Arya, *J. Energy Chem.*, 2022, **68**, 330-386.
37. W. Yan, S. Ye, Y. Li, W. Sun, H. Rao, Z. Liu, Z. Bian and C. Huang, *Adv. Energy Mater.*, 2016, **6**, 1600474.
38. J. Zhou, H. Li, L. Tan, Y. Liu, J. Yang, R. Hua and C. Yi, *Angew. Chem. Int. Ed.*, 2023, **62**, e202300314.
39. J. Xia, P. Luizys, M. Daskeviciene, C. Xiao, K. Kantminiene, V. Jankauskas, K. Rakstys, G. Kreiza, X.-X. Gao, H. Kanda, K. G. Brooks, I. R. Alwani, Q. U. Ain, J. Zou, G. Shao, R. Hu, Z. Qiu, A. Slonopas, A. M. Asiri, Y. Zhang, P. J. Dyson, V. Getautis and M. K. Nazeeruddin, *Adv. Mater.*, 2023, **35**, 2300720.
40. Y. Li, *Sci. China Chem.*, 2023, **66**, 2155-2156.
41. S. Li, W. Chen, Y. Yang, P. Zhao, H. Cui, Y. Huang, D. He, Y. Ning, Y. Feng and B. Zhang, *Solar RRL*, 2023, **7**, 2300252.
42. D. W. Kim, K.-H. Choi, S. H. Hong, H.-S. Kang, J. E. Kwon, S. Park, B.-K. An and S. Y. Park, *Adv. Energy Mater.*, 2023, **13**, 2300219.
43. S. Collavini, A. Cabrera-Espinoza and J. L. Delgado, *Macromolecules*, 2021, **54**, 5451-5463.
44. S. F. Völker, M. Vallés-Pelarda, J. Pascual, S. Collavini, F. Ruipérez, E. Zuccatti, L. E. Hueso, R. Tena-Zaera, I. Mora-Seró and J. L. Delgado, *Chem. Eur. J.*, 2018, **24**, 8524-8529.
45. D. Chandrasekaran, W.-H. Chiu, K.-M. Lee, J.-M. Liao, H.-H. Chou and Y.-S. Yen, *Journal*, 2022, **14**, 1580.
46. Z. Deng, S. Cui, K. Kou, D. Liang, X. Shi and J. Liu, *Front. Chem.*, 2021, **9**.
47. M. M. H. Desoky, M. Bonomo, R. Buscaino, A. Fin, G. Viscardi, C. Barolo and P. Quagliotto, *Energies*, 2021, **14**, 2279.
48. L. Duan, Y. Chen, J. Yuan, X. Zong, Z. Sun, Q. Wu and S. Xue, *Dyes Pigm.*, 2020, **178**, 108334.
49. Y.-C. Chen, D.-Z. Lin, J.-C. Wang, J.-S. Ni, Y.-Y. Yu and C.-P. Chen, *Mater. Chem. Front.*, 2021, **5**, 1373-1387.
50. E. Sheibani, L. Yang and J. Zhang, *Sol. RRL*, 2020, **4**, 2000461.
51. L. M. Nhari, R. M. El-Shishtawy and A. M. Asiri, *Dyes Pigm.*, 2021, **193**, 109465.
52. S. B. Akula, C. Su, Y. S. Tingare, H.-C. Lan, Y.-J. Lin, Y.-T. Wang, Y.-C. Jheng, X.-C. Lin, Y.-C. Chang and W.-R. Li, *J. Mater. Chem. C*, 2020, **8**, 16577-16583.
53. F. M. Rombach, S. A. Haque and T. J. Macdonald, *Energy Environ. Sci.*, 2021, **14**, 5161-5190.
54. L. Groenendaal, F. Jonas, D. Freitag, H. Pielartzik and J. R. Reynolds, *Adv. Mater.*, 2000, **12**, 481-494.
55. Y. Fang, X. Wang, Q. Wang, J. Huang and T. Wu, *phys. status solidi A*, 2014, **211**, 2809-2816.

56. J. Yang, B. D. Siempelkamp, D. Liu and T. L. Kelly, *ACS Nano*, 2015, **9**, 1955-1963.
57. C. Huang, W. Fu, C.-Z. Li, Z. Zhang, W. Qiu, M. Shi, P. Heremans, A. K. Y. Jen and H. Chen, *J. Am. Chem. Soc.*, 2016, **138**, 2528-2531.
58. K. Rakstys, M. Saliba, P. Gao, P. Gratia, E. Kamarauskas, S. Paek, V. Jankauskas and M. K. Nazeeruddin, *Angew. Chem. Int. Ed.*, 2016, **55**, 7464-7468.
59. K. Rakstys, S. Paek, P. Gao, P. Gratia, T. Marszalek, G. Grancini, K. T. Cho, K. Genevicius, V. Jankauskas, W. Pisula and M. K. Nazeeruddin, *J. Mater. Chem. A*, 2017, **5**, 7811-7815.
60. I. García-Benito, I. Zimmermann, J. Urieta-Mora, J. Aragó, J. Calbo, J. Perles, A. Serrano, A. Molina-Ontoria, E. Ortí, N. Martín and M. K. Nazeeruddin, *Adv. Funct. Mater.*, 2018, **28**, 1801734.
61. Z. a. Zhou, X. Zhang, R. Ghadari, X. Liu, W. Wang, Y. Ding, M. Cai, J. H. Pan and S. Dai, *Sol. Energy*, 2021, **221**, 323-331.
62. P. Murugan, T. Hu, X. Hu and Y. Chen, *J. Mater. Chem. A*, 2022, **10**, 5044-5081.
63. F. Wu, Y. Shan, J. Qiao, C. Zhong, R. Wang, Q. Song and L. Zhu, *ChemSusChem*, 2017, **10**, 3833-3838.
64. S. S. Reddy, V. M. Arivunithi, V. G. Sree, H. Kwon, J. Park, Y.-C. Kang, H. Zhu, Y.-Y. Noh and S.-H. Jin, *Nano Energy*, 2019, **58**, 284-292.
65. B. Xu, Z. Zhu, J. Zhang, H. Liu, C.-C. Chueh, X. Li and A. K.-Y. Jen, *Adv. Energy Mater.* , 2017, **7**, 1700683.
66. H. Cheng, Y. Li, G. Zhao, K. Zhao and Z.-S. Wang, *ACS Appl. Mater. Interfaces*, 2019, **11**, 28960-28967.
67. L. Liu, F. Li, C. Zhao, F. Bi, T. Jiu, M. Zhao, J. Li, G. Zhang, L. Wang, J. Fang and X. Xiao, *ACS Appl. Energy Mater.*, 2019, **2**, 6577-6583.
68. P. Xu, P. Liu, Y. Li, B. Xu, L. Kloo, L. Sun and Y. Hua, *ACS Appl. Mater. Interfaces*, 2018, **10**, 19697-19703.
69. Z. Gong, R. Wang, Y. Jiang, X. Kong, Y. Lin, Z. Xu, G. Zhou, J.-M. Liu, K. Kempa and J. Gao, *Org. Electron.*, 2021, **92**, 106102.
70. Z.-Z. Sun, S. Feng, W.-L. Ding, X.-L. Peng, J.-L. Liu and X.-L. Xu, *Sol. Energy*, 2021, **224**, 491-499.
71. B.-B. Cui, C. Zhu, S. Yang, Y. Han, N. Yang, L. Zhang, Y. Wang, Y. Jia, L. Zhao and Q. Chen, *ACS Omega*, 2018, **3**, 10791-10797.
72. J. Chen, J. Xia, W.-J. Gao, H.-J. Yu, J.-X. Zhong, C. Jia, Y.-S. Qin, Z. She, D.-B. Kuang and G. Shao, *ACS Appl. Mater. Interfaces*, 2020, **12**, 21088-21099.
73. L. Nakka, Y. Cheng, A. G. Aberle and F. Lin, *Adv. Energy Sustainability Res.*, 2022, **3**, 2200045.
74. S. Liu, X. Yi, H. Wang, T. Ye, K. Wang, W. Cao, J. Guan, R. Fan, Y. Yang, S. Hao and D. Xia, *Front. Chem.*, 2022, **10**, 898320.
75. F. Liu, F. Wu, W. Ling, L. Zhu, Q. Li and Z. Li, *Sol. RRL*, 2021, **5**, 2100070.
76. S. B. Akula, C. Su, Y.-T. Wang, Y. S. Tingare, B.-R. Chen, Y.-C. Jheng, Y.-J. Lin, H.-C. Lan, Y.-C. Chang, W. Lekphet and W.-R. Li, *J. Power Sources*, 2021, **483**, 229177.
77. W. Jiang, H. Di, H. Sun, C. Zhao, F. Liao and Y. Zhao, *J. Cryst. Growth*, 2020, **550**, 125880.
78. Y. Xia, C. Zhao, P. Zhao, L. Mao, Y. Ding, D. Hong, Y. Tian, W. Yan and Z. Jin, *J. Power Sources*, 2021, **494**, 229781.
79. F. Cheng, J. Zhang and T. Pauporté, *ChemSusChem*, 2021, **14**, 3665-3692.
80. M. Cheng, K. Aitola, C. Chen, F. Zhang, P. Liu, K. Sveinbjörnsson, Y. Hua, L. Kloo, G. Boschloo and L. Sun, *Nano Energy*, 2016, **30**, 387-397.
81. C.-Y. Chang, H.-H. Huang, H. Tsai, S.-L. Lin, P.-H. Liu, W. Chen, F.-C. Hsu, W. Nie, Y.-F. Chen and L. Wang, *Adv. Sci.*, 2021, **8**, 2002718.
82. C.-G. Wu, C.-H. Chiang and S. H. Chang, *Nanoscale*, 2016, **8**, 4077-4085.
83. J. D. Servaites, M. A. Ratner and T. J. Marks, *Energy Environ. Sci.*, 2011, **4**, 4410-4422.
84. Y. Cheng, Q. Fu, X. Zong, Y. Dong, W. Zhang, Q. Wu, M. Liang, Z. Sun, Y. Liu and S. Xue, *J. Chem. Eng.*, 2021, **421**, 129823.
85. F. Tamaddon*, A. D. Tafti and F. Pooramini., *Synthesis*, 2016, **48**, 4295-4299.
86. Y. S. Tingare, Nguyên, S. n. Vinh, H.-H. Chou, Y.-C. Liu, Y.-S. Long, T.-C. Wu, T.-C. Wei and C.-Y. Yeh, *Adv. Energy Mater.*, 2018, **8**, 1802405.
87. L. She, M. Liu and D. Zhong, *ACS Nano*, 2016, **10**, 1126-1131.
88. C. Hanmandlu, R. Paste, H. Tsai, S. N. S. Yadav, K.-W. Lai, Y.-Y. Wang, C. S. Gantepogu, C.-H. Hou, J.-J. Shyue, Y.-J. Lu, T. S. Jadhav, J.-M. Liao, H.-H. Chou, H. Q. Wong, T.-J. Yen, C.-S. Lai, D. Ghosh, S. Tretiak, H.-J. Yen and C.-W. Chu, *Nano Energy*, 2023, **107**, 108136.
89. H. Tsai, D. Ghosh, W. Panaccione, L.-Y. Su, C.-H. Hou, L. Wang, L. R. Cao, S. Tretiak and W. Nie, *ACS Energy Lett.*, 2022, **7**, 3871-3879.
90. H.-H. Huang, H. Tsai, R. Raja, S.-L. Lin, D. Ghosh, C.-H. Hou, J.-J. Shyue, S. Tretiak, W. Chen, K.-F. Lin, W. Nie and L. Wang, *ACS Energy Lett.*, 2021, **6**, 3376-3385.
91. J. Wang and W.-J. Yin, *J. Phys. Chem. Lett.*, 2022, **13**, 6694-6700.
92. D. Meggiolaro, E. Mosconi and F. De Angelis, *ACS Energy Lett.*, 2019, **4**, 779-785.
93. M. L. Agiorgousis, Y.-Y. Sun, H. Zeng and S. Zhang, *J. Am. Chem. Soc.*, 2014, **136**, 14570-14575.
94. D. Ghosh, A. Aziz, J. A. Dawson, A. B. Walker and M. S. Islam, *Chem. Mater.*, 2019, **31**, 4063-4071.
95. F. Tamaddon, A. D. Tafti and F. Pooramini., *Synthesis*, 2016, **48**, 4295-4299.
96. G. Kresse and J. Hafner, *Phys. Rev. B*, 1993, **47**, 558-561.
97. G. Kresse and J. Hafner, *Phys. Rev. B*, 1994, **49**, 14251-14269.
98. G. Kresse and D. Joubert, *Phys. Rev. B*, 1999, **59**, 1758-1775.
99. J. P. Perdew, K. Burke and M. Ernzerhof, *Phys. Rev. Lett.*, 1996, **77**, 3865-3868.
100. S. Grimme, J. Antony, S. Ehrlich and H. Krieg, *J. Chem. Phys.*, 2010, **132**.